Supplementary Material
Confinement-induced drift in Marangoni-driven transport of surfactant: a Lagrangian perspective

Richard Mcnair[1]†, Oliver E. Jensen‡ [1] and Julien R. Landel¶ [1,2]

[1]Department of Mathematics, University of Manchester, Oxford Road, M13 9PL, UK

[2]Universite Claude Bernard Lyon 1, Laboratoire de Mecanique des Fluides et d'Acoustique (LMFA), UMR5509, CNRS, Ecole Centrale de Lyon, INSA Lyon, 69622 Villeurbanne, France

S1. Full definition of ξ for the solution of the three-deposits problem using the Lagrangian method

In the problem presented in §2.2.2, to obtain the deformed Lagrangian coordinate ξ (see (2.24)), we need to consider 9 regions of Ω (see figure 2a). We also impose that the line $\xi = 0$ maps to the line $x = 0$. Hence,

$$\xi = \begin{cases} \delta x & \text{in R1,} \\ x - \left(\frac{(x-6)^3}{3} + x(y-2)^2 \right)(1-\delta) + \frac{2}{3}(1-\delta)(y-1)(3-y)(\sqrt{(y-1)(3-y)} - 9) & \text{in R2,} \\ \delta x + \frac{4}{3}(1-\delta)((y-1)(3-y))^{3/2} & \text{in R3,} \\ x - \frac{1}{4}\left(\frac{(x-10)^3}{3} + x(y-5)^2 \right)(1-\delta) + \frac{1}{6}(1-\delta)(y-3)(7-y)(\sqrt{(y-3)(7-y)} - 15) & \text{in R4,} \\ \delta x + \frac{1}{3}(1-\delta)((y-3)(7-y))^{3/2} & \text{in R5,} \\ 2x - \frac{1}{9}\left(\frac{(x-4)^3}{3} + x(y-7)^2 \right)(2-\delta) + \frac{2}{27}(2-\delta)(y-4)(10-y)(\sqrt{(y-4)(10-y)} - 6) & \text{in R6,} \\ \delta x + \frac{4}{27}(2-\delta)((y-4)(10-y))^{3/2} & \text{in R7,} \\ x - \frac{1}{4}\left(\frac{(x-10)^3}{3} + x(y-5)^2 \right)(1-\delta) \\ \quad + \frac{1}{6}(1-\delta)(y-3)(7-y)(\sqrt{(y-3)(7-y)} - 15) + \frac{4}{27}(2-\delta)((y-4)(10-y))^{3/2} & \text{in R8,} \\ \delta x + \frac{1}{3}(1-\delta)((y-3)(7-y))^{3/2} + \frac{4}{27}(2-\delta)((y-4)(10-y))^{3/2} & \text{in R9.} \end{cases}$$

(S1.1)

We now describe the coordinates of the boundaries and edges of circular deposits in the deformed Lagrangian coordinates. Three of the four Lagrangian boundaries are $0 \leqslant \xi \leqslant 13\delta$ for both $\eta = 0$ and $\eta = 11$, and $0 \leqslant \eta \leqslant 11$ for $\xi = 0$. The fourth boundary $\partial\Omega_R$

† Email address for correspondence: richard.mcnair@manchester.ac.uk
‡ Email address for correspondence: oliver.jensen@manchester.ac.uk
¶ Email address for correspondence: julien.landel@manchester.ac.uk

(the right hand side boundary of the deformed domain shown in figure 2b) is given by

$$\xi = 13\delta, \qquad\qquad\qquad 0 \leqslant \eta \leqslant 1 \text{ for R1,} \tag{S1.2a}$$

$$\xi = 13\delta + \tfrac{4}{3}(1-\delta)((\eta-1)(3-\eta))^{3/2} \qquad\qquad 1 < \eta \leqslant 3 \text{ for R3,} \tag{S1.2b}$$

$$\xi = 13\delta + \tfrac{1}{3}(1-\delta)((\eta-3)(7-\eta))^{3/2} \qquad\qquad 3 < \eta \leqslant 4 \text{ for R5,} \tag{S1.2c}$$

$$\xi = 13\delta + \tfrac{1}{3}(1-\delta)((\eta-3)(7-\eta))^{3/2} + \tfrac{4}{27}(2-\delta)((\eta-4)(10-\eta))^{3/2} \qquad 4 < \eta \leqslant 7 \text{ for R9,} \tag{S1.2d}$$

$$\xi = 13\delta + \tfrac{4}{27}(2-\delta)((\eta-4)(10-\eta))^{3/2} \qquad\qquad 7 < \eta \leqslant 10 \text{ for R7,} \tag{S1.2e}$$

$$\xi = 13\delta \qquad\qquad\qquad 10 < \eta \leqslant 11 \text{ for R1.} \tag{S1.2f}$$

The boundaries of the three deposits are given by

$$\xi = \delta(6 - \sqrt{1-(\eta-2)^2}) \quad\text{and}\quad \delta(6 + \sqrt{1-(\eta-2)^2}) + \tfrac{4}{3}(1-\delta)((\eta-1)(3-\eta))^{3/2} \quad\text{with}\quad 1 \leqslant \eta \leqslant 3, \tag{S1.3}$$

for R2,

$$\xi = \delta(10 - \sqrt{4-(\eta-5)^2}) \quad\text{and}\quad \delta(10 + \sqrt{4-(\eta-5)^2}) + \tfrac{1}{3}(1-\delta)((\eta-3)(7-\eta))^{3/2} \quad\text{with}\quad 3 \leqslant \eta \leqslant 4, \tag{S1.4}$$

for R4,

$$\delta(10 - \sqrt{4-(\eta-5)^2}) + \tfrac{4}{27}(2-\delta)((\eta-4)(10-\eta))^{3/2}$$

$$\text{and}\quad \delta(10 + \sqrt{4-(\eta-5)^2}) + \tfrac{1}{3}(1-\delta)((\eta-3)(7-\eta))^{3/2} + \tfrac{4}{27}(2-\delta)((\eta-4)(10-\eta))^{3/2} \quad\text{with}\quad 4 \leqslant \eta \leqslant 7, \tag{S1.5}$$

for R8,

$$\xi = \delta(4 - \sqrt{9-(\eta-7)^2}) \quad\text{and}\quad \delta(4 + \sqrt{9-(\eta-7)^2}) + \tfrac{4}{27}(2-\delta)((\eta-4)(10-\eta))^{3/2} \quad\text{with}\quad 4 \leqslant \eta \leqslant 10. \tag{S1.6}$$

for R6.

S2. Eulerian and Lagrangian comparison

Figure S1 overlays the contours of both components of the map found from Eul[0.25] and Lag[0.25]. Both solutions are at $t = t_f$, a time found from consideration of (B12) implemented during the calculation of Eul[0.25], such that both X_{tol} and Y_{tol} were set to 10^{-3}. Both sets of contours in figure S1 coincide with each other, apart from small regions in figure S1(a) where small oscillations occur on the magenta contours (see, e.g., for $7 \leqslant x_0 \leqslant 11$ and $8 \leqslant y_0 \leqslant 10$). The fact that these oscillations occur for X, and not for Y is evidence that they are an artefact caused by the deformation of the Lagrangian domain (figure 2), which is implemented in the x_0 coordinate direction only.

S3. The evolution of the concentration field in time

In figure S2 we present a time series of colour maps of the concentration field Γ taken from Eul[0.25]. This concentration evolution is calculated from (2.1), from initial conditions (2.7, 2.9) for $\delta = 0.25$, $(x_1, y_1) = (6, 2)$, $(x_2, y_2) = (10, 5)$, $(x_3, y_3) = (4, 7)$,
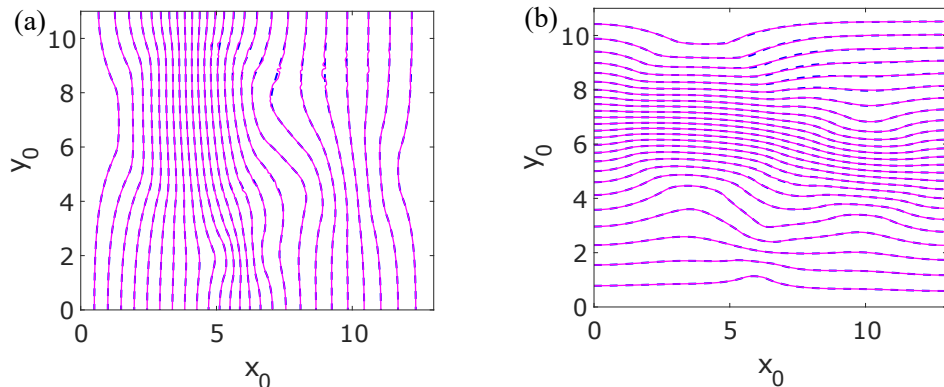
Figure S1: Graphs (a) and (b) show the overlay of the X and Y components, respectively, of the maps taken from Eul[0.25] and Lag[0.25]. The solution from Eul[0.25] is given by the dashed blue contours, and the solution from Lag[0.25] is given by the solid magenta contours.
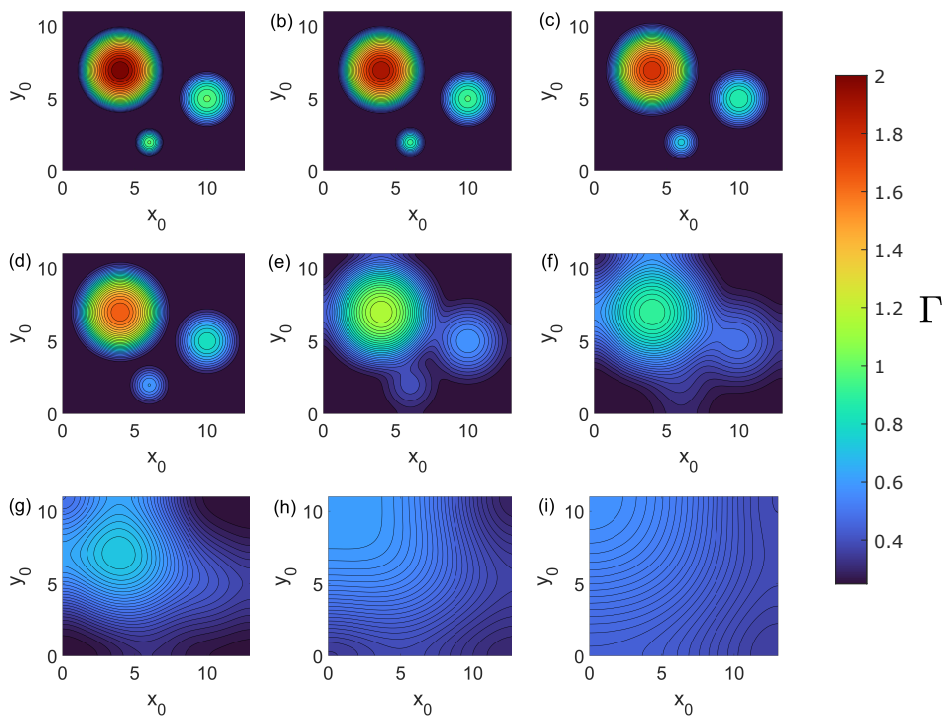

Figure S2: The concentration evolution over time given as a colour map for Γ taken from Eul[0.25], shown at $t = 0$ in (a), $t = 0.1$ in (b), $t = 0.5$ in (c), $t = 1$ in (d), $t = 5$ in (e), $t = 10$ in (f), $t = 20$ in (g), $t = 50$ in (h), and $t = 100$ in (i).

$r_2 = 2$, $r_3 = 3$, $\Gamma_2 = 1$ and $\Gamma_3 = 2$. This solution terminates at $t_f = 1047.8$ as stated in table 1, but here we see the concentration field is smoothed to a shallow gradient between top-left and bottom-right corners by $t = 100$ (panel i).

S4. Comparison between the Eulerian particle-tracking solution in the steady-state and the Monge–Ampère solution

Figure S3 shows a comparison between the final particle locations found by both the finite-difference Eulerian solution and the Monge–Ampère approximation for the three-deposit problem (see §2.1.2). Figures S3(a) and S3(b) show the normalized absolute error defined as (2.34) in the main text, while figures S3(c) and S3(d) show a relative error defined as

$$||X_{EU} - X_{MA}|| = \frac{\sqrt{(X_{EU} - X_{MA})^2 + (Y_{EU} - Y_{MA})^2}}{\sqrt{(X_{EU} - x_0)^2 + (Y_{EU} - y_0)^2}}. \qquad (S4.1)$$

The relative error normalizes the absolute error with respect to the distance travelled by each particle using the Eulerian method. Note that the relative error diverges near fixed points where $\mathbf{X}_{EU}(t_f) \approx (x_0, y_0)$.

For moderate δ, the error is very small everywhere except for a few places in the region initially occupied by endogenous surfactant where a significant rotational part of the map is acquired due to deposits interacting with each other and with boundaries. A larger error exists near fixed points of Eul[0.25]. For $\delta = 0.002$ the error is larger than for $\delta = 0.25$, but even for small δ, the difference between the two solutions is close to zero in most of the domain, and especially inside the exogenous deposits.

Figure S4 shows $\nabla^2_{x_0}\psi/\nabla^2_{x_0}\phi$ for Eul[0.25] and Eul[0.002]; the data provide evidence supporting the claim (2.30) from the main text which implies that $\nabla^2_{x_0}\psi \ll \nabla^2_{x_0}\phi$, given the boundary conditions (2.29). The evidence is weaker for $\delta = 0.002$, although the inequality holds in most parts of the domain.

S5. Statistics for the difference in particle location for different drop configurations

Figures S5, S6 and S7 show box-and-whisker plots for a variety of different exogenous deposit configurations (see table S1) not considered in the main paper to provide further quantitative comparison between the Monge–Ampère method and the Eulerian solution (assumed to be close to the exact solution). While quadratic concentration profiles are considered in the main paper, and cosine profiles in Appendix F, here we also consider linear and top-hat shaped initial concentration profiles within circular deposits. Cosine shaped circular deposits with centres at $\mathbf{x}_c = (x_c, y_c)$, radii r and maximum concentration $\Gamma_{0,c}$ are given by (F1) in the main text, linear concentration profiles within the circular deposits are given by

$$\mathcal{C}_l(\mathbf{x}_0; \mathbf{x}_c, r, \Gamma_{0,c} - \delta) = \begin{cases} (\Gamma_{0,c} - \delta)\left(1 - \frac{|\mathbf{x}_0 - \mathbf{x}_c|}{r}\right) & |\mathbf{x}_0 - \mathbf{x}_c| \leqslant r \\ 0 & |\mathbf{x}_0 - \mathbf{x}_c| > r \end{cases}, \qquad (S5.1)$$

and top-hat shaped profiles are given by

$$\mathcal{C}_t(\mathbf{x}_0; \mathbf{x}_c, r, \Gamma_{0,c} - \delta) = \begin{cases} \Gamma_{0,c} - \delta & |\mathbf{x}_0 - \mathbf{x}_c| \leqslant r \\ 0 & |\mathbf{x}_0 - \mathbf{x}_c| > r \end{cases}. \qquad (S5.2)$$

In the case of a one-deposit problem, with initial conditions described in table S1, figure S5 shows that a single deposit configuration (shown in figure S5a) produces a larger median error (shown in figure S5b) when the deposit is initially placed closer to a corner of the domain, and the median error decreases as the deposit approaches the centre of the domain. Nevertheless, we find that overall the maximum distance error is
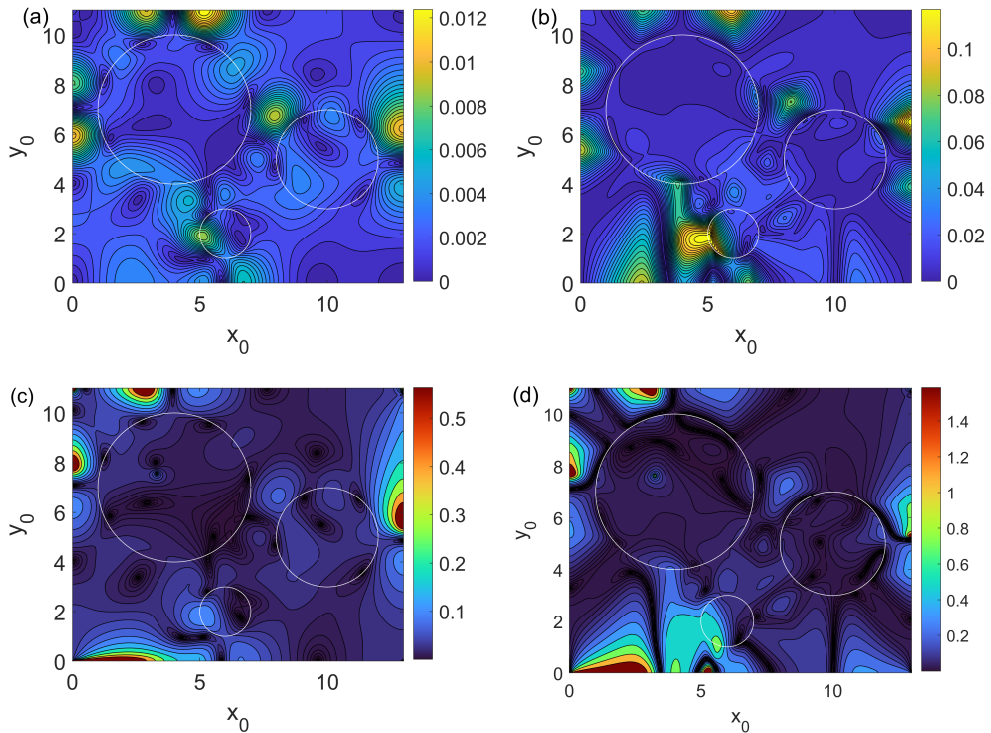
Figure S3: Contour plots of the Euclidean distance between predictions of final particle location from the Eulerian particle-tracking and the Monge–Ampère methods, as functions of Lagrangian coordinates for the three-deposits problem (see §2.1.2). (a) Shows the normalized absolute error $|X_{EU} - X_{MA}|/L_1$ for Eul[0.25] and MA[0.25], (b) shows the same for Eul[0.002] and MA[0.002]. (c) Shows the relative error $||X_{EU} - X_{MA}||$ (see (S4.1)) for Eul[0.25] and MA[0.25] with contours spaced logarithmically, and (d) shows the same for Eul[0.002] and MA[0.002]. White circles show the initial deposit locations (see figure 2a).
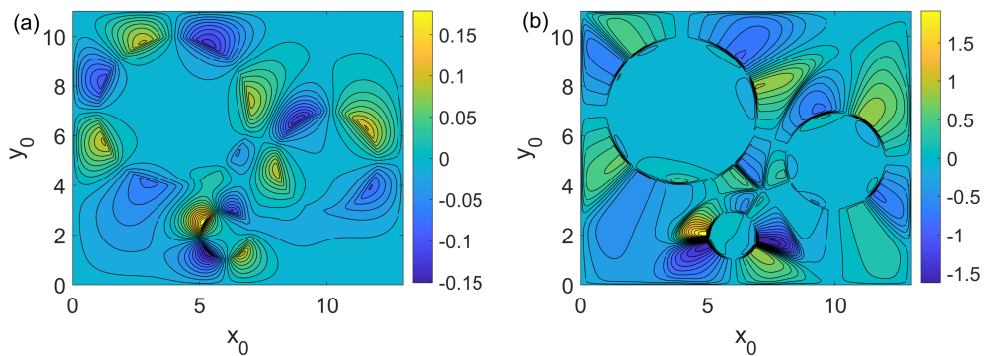

Figure S4: Contour plots showing the ratio $\nabla^2_{x_0}\psi / \nabla^2_{x_0}\phi$ for Eul[0.25] in (a) and Eul[0.002] in (b).

Method	δ	No. of deposits	Dep. centres (x_c, y_c) 1/2/3	Dep. radii r 1/2/3	Max conc. $\Gamma_{0,c}$ 1/2/3	Profile shape	Key
EU	0.25	1	Various/NA/NA	1/NA/NA	1/NA/NA	Cosine	NA
MA	0.25	1	Various/NA/NA	1/NA/NA	1/NA/NA	Cosine	NA
EU	0.25	2	Various/Various/NA	1/1/NA	1/1/NA	Cosine	NA
MA	0.25	2	Various/Various/NA	1/1/NA	1/1/NA	Cosine	NA
EU	0.25	3	(6,2)/(10,5)/(4,7)	1/2/3	1/1/2	Cosine	$\text{Eul}_c[0.25]$
MA	0.25	3	(6,2)/(10,5)/(4,7)	1/2/3	1/1/2	Cosine	$\text{MA}_c[0.25]$
EU	0.25	3	(6,2)/(10,5)/(4,7)	1/2/3	1/1/2	Quadratic	$\text{Eul}[0.25]$
MA	0.25	3	(6,2)/(10,5)/(4,7)	1/2/3	1/1/2	Quadratic	$\text{MA}[0.25]$
EU	0.25	3	(6,2)/(10,5)/(4,7)	1/2/3	$\frac{11}{8}/\frac{11}{8}/\frac{23}{8}$	Linear	$\text{Eul}_L[0.25]$
MA	0.25	3	(6,2)/(10,5)/(4,7)	1/2/3	$\frac{11}{8}/\frac{11}{8}/\frac{23}{8}$	Linear	$\text{MA}_L[0.25]$
EU	0.25	3	(6,2)/(10,5)/(4,7)	1/2/3	$\frac{5}{8}/\frac{5}{8}/\frac{9}{8}$	Top Hat	$\text{Eul}_T[0.25]$
MA	0.25	3	(6,2)/(10,5)/(4,7)	1/2/3	$\frac{5}{8}/\frac{5}{8}/\frac{9}{8}$	Top Hat	$\text{MA}_T[0.25]$

Table S1: Table showing the various simulations studied in §S5. The only methods considered here are Eulerian particle tracking (EU) and Monge–Ampère (MA). We consider a variety of one- and two-deposit configurations with centres of the deposits reported in figures S5 and S6. We consider the three-deposit problem for a variety of different initial concentration profile shapes, with the maximum concentration $\Gamma_{0,c}$ within each deposit chosen such that the mass of surfactant is the same in each deposit for each method.

largely insensitive to drop location. The error is bounded above by 0.002 for $\delta = 0.25$, which corresponds to 0.2% of the domain length L_1.

Figure S6 shows a variety of independent two-deposit configurations, with initial conditions described in table S1. As in figure S5 the most asymmetric configurations have the largest median error, and the error decreases slightly with increasing symmetry of the initial configuration. All distance errors in these examples are bounded above by 0.005, corresponding to 0.5% of the domain length.

Figure S7 shows particle data for the three-deposits problem considered in §(2.1.2), where the initial concentration distribution has the profile shown on the x-axis, varying from a cosine (F1), a linear (S5.1), a quadratic (2.8) and a top-hat (S5.2) profile. The largest median discrepancy between the Monge–Ampère and the Eulerian solution is found for the profiles with the more complicated first derivative (the cosine profile), despite the cosine profile being the smoothest of the shown profiles. In all the examples, the maximum distance error is bounded above by 0.02, corresponding to 2% of the domain length.

Figures S5, S6 and S7 show little variation in the error between the two methods. The specific configuration of a fixed number of deposits, the initial shape of the profiles within the deposits do not seem to affect much the error between MA and EU methods. Overall, we find that the parameters which tend to increase the most significantly the error between the two methods are the endogenous surfactant concentration δ, and the number of deposits.
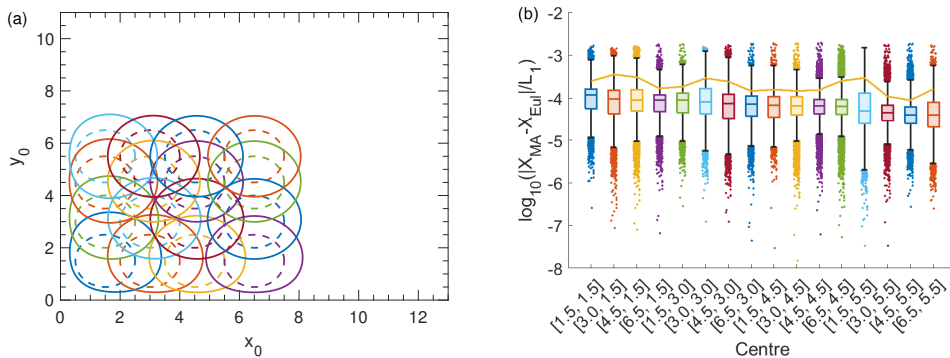
Figure S5: Graphs showing results for the one-deposit problem which consists of a single deposit of unit radius and initial concentration profile $\delta + \mathcal{C}_c(x_c, y_c, 1, 1 - \delta)$ spreading to equilibrium, with $[x_c, y_c]$ shown on the x-axis and for $\delta = 0.25$ ($\mathcal{C}_c$ is defined in (F1) in the main text). (a) Shows the 16 different initial boundaries of the single deposits as dashed lines, with final locations of the boundaries found by the Eulerian particle-tracking method as solid lines. (b) Shows box and whisker plots of the logarithm of $|X_{EU} - X_{MA}|/L_1$, where each data point corresponds to a unique initial particle location calculated from a uniformly-spaced grid, and each plot is colour-coded to match (a). The orange curve denotes the 90th percentile of each solution. Owing to symmetry considerations, we have showed only initial deposit locations in one quadrant of the domain. The plots in (b) are ordered by descending median. Outliers are plotted as a cloud of points above and below the whiskers.
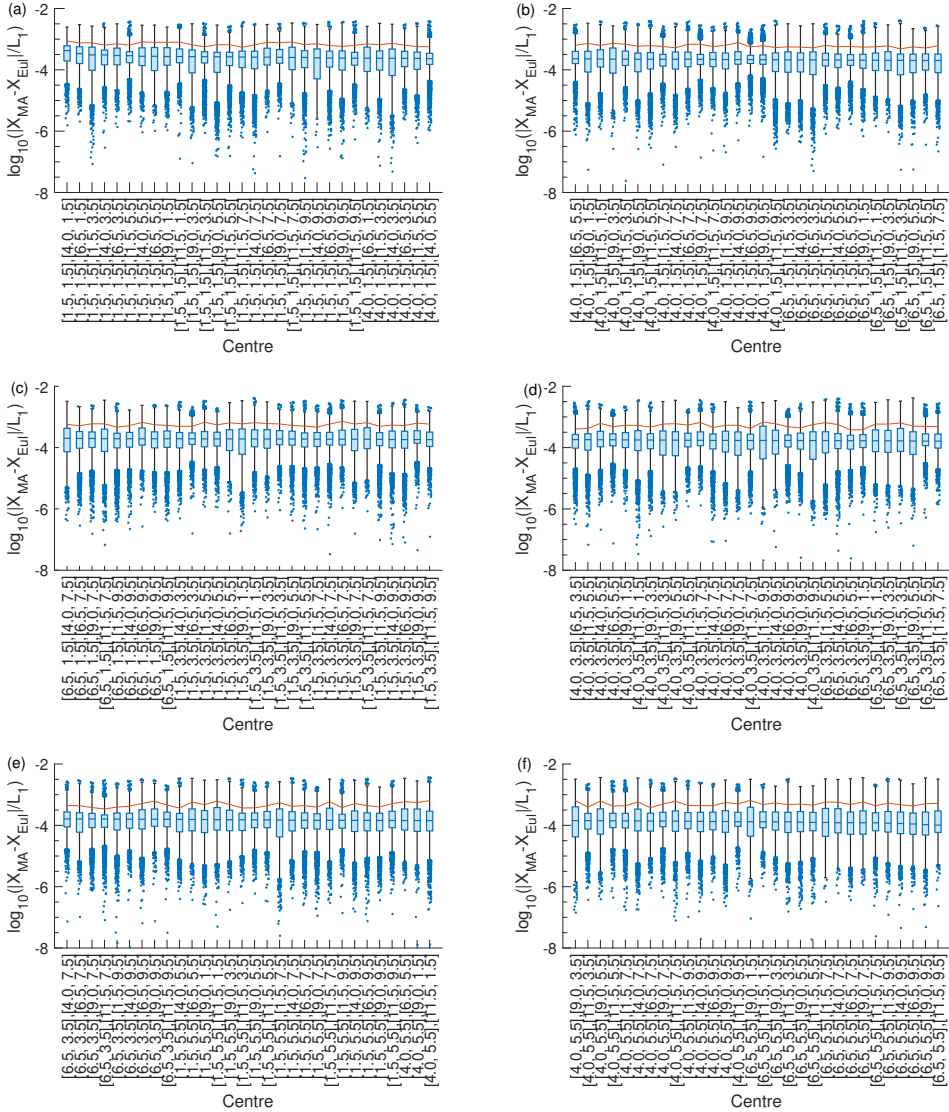
Figure S6: Box and whisker plots of the logarithm of the normalized absolute error $|X_{EU} - X_{MA}|/L_1$ between the predictions of final particle location for the Eulerian particle tracking and Monge–Ampère methods for two deposits of unit radius. The initial concentration profile is $\delta + \mathcal{C}_c(x_{c1}, y_{c1}, 1, 1 - \delta) + \mathcal{C}_c(x_{c2}, y_{c2}, 1, 1 - \delta)$, with $[x_{c1}, y_{c1}], [x_{c2}, y_{c2}]$ indicated on the x-axis, and $\delta = 0.25$. Each box plot is for a unique two-deposit configuration, and each data point corresponds to a unique initial particle location taken from an evenly spaced grid. Graphs are ordered by descending median. The orange curve shows the 90th percentiles. Outliers are plotted as a cloud of points above and below the whiskers.
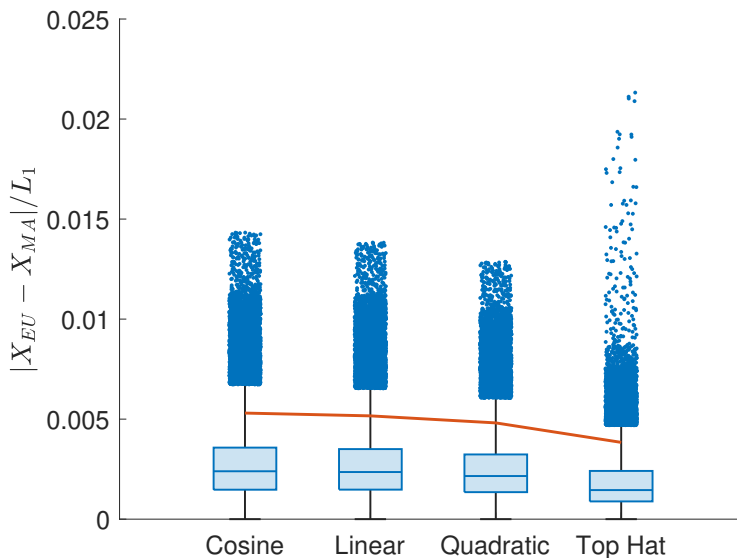
Figure S7: Graph showing box and whisker plots for the normalised absolute error between predictions of final particle location from the Eulerian particle-tracking and Monge–Ampère methods, where each data point is a unique starting location taken from an evenly spaced grid. The graph plots $|X_{EU} - X_{MA}|/L_1$ for the three-deposit problem considered in the main paper (see §2.2.2), but where the exogenous deposits concentration profiles have different initial shapes as indicated on the x-axis. For the cosine profiles, $\mathcal{C}_q$ in (2.9) of the main text is replaced by $\mathcal{C}_c$ (equation (F1)) for a cosine profile with $\Gamma_{0,c} = 1$ for the smallest two deposits and $\Gamma_{0,c} = 2$ for the largest deposit. For the linear profile, $\mathcal{C}_q$ is replaced by $\mathcal{C}_l$ (equation (S5.1)) with $\Gamma_{0,c} = 11/8$ for the smallest two deposits and $\Gamma_{0,c} = 23/8$ for the largest deposit. Lastly, for the top hat profile, $\mathcal{C}_q$ is replaced by $\mathcal{C}_t$ (equation (S5.2)) with $\Gamma_{0,c} = 5/8$ for the smallest two deposits and $\Gamma_{0,c} = 11/8$ for the largest. These choices of $\Gamma_{0,c}$ yield the same total mass of exogenous surfactant between all the simulations. The orange curve denotes the 90th percentile of each solution. Outliers are plotted as a cloud of points above the top whisker.